Available online at www.sciencedirect.com
SCIENCE DIRECT®
Journal of Power Sources 124 (2003) 487–498
JOURNAL OF POWER SOURCES
www.elsevier.com/locate/jpowsour

Simulation of the chemical/electrochemical reactions and heat/mass transfer for a tubular SOFC in a stack

Pei-Wen Li*, Minking K. Chyu

Department of Mechanical Engineering, University of Pittsburgh, Benedum Engineering Hall, Pittsburgh, PA 15232, USA

Received 18 June 2003; accepted 30 June 2003

Abstract

The heat and species transport processes in a tubular type solid oxide fuel cell (SOFC) that works in a cell stack were analyzed and modeled. Since most of the single tubular SOFCs working in a cell stack share the same/similar chemical/electrochemical and heat/mass transfer conditions, it is plausible to assume that heat and species are not exchanged between one cell and its neighboring cells. Therefore, a surrounding fuel flow space was outlined controllable by a specific single cell, for which zero flux was assumed at its boundary in neighborhood with other cells. The numerical model subjects such a cell and its controllable fuel flow space to a two-dimensional analysis for the flow, heat/mass transfer and chemical/electrochemical performance. Computations were performed for three different tubular SOFCs having practical operating results available from publications by different researchers. The numerical results of the terminal voltages for those different SOFCs showed very good agreement with the published experimental data. It is expectable that the proposed numerical model be used to significantly help the design and operation of a SOFC stack in practical applications.

Keywords: Chemical/electrochemical reactions; Heat/mass transfer; Tubular SOFC; Simulation

1. Introduction

A solid oxide fuel cell (SOFC) is one of the most promising type of fuel cells currently being considered to be used as a power source for automobiles and stationary power plants [1,2]. A SOFC has a oxide-ion-conductive electrolyte and works by the oxidation of a fuel at the anode side. Both carbon monoxide and hydrogen can serve as fuels, which provides the SOFC with an advantage in fuel adaptability. For maintaining the high oxide-ion conductivity of the solid oxide electrolyte, SOFCs must operate at a high temperature of 800–1000 °C. This also provides SOFCs with another advantage in that natural gas can be reformed in the cell stack [3,4].

A SOFC essentially consists of two porous electrodes separated by a dense, gas-tight, oxide-ion-conducting electrolyte. Planar and tubular geometries are the two popular designs for solid oxide fuel cells. The technique of designing and manufacturing a tubular type SOFC is relatively mature, and it is possible to construct a medium and large scale cell stack for automobile and stationary power generation. There have been growing experimental test results on the overall electrochemical performance for tubular type SOFCs. However, it is still far from enough to guide the design and operation of a solid oxide fuel cell, especially the cell stack. To meet the need of understanding the operational details and the internal temperature and species' mass fraction parameters when a fuel cell works in a cell stack, the present study develops a reliable numerical model validated by available experimental data. Localized experimental measurements in a SOFC working at high temperature is difficult, so numerical analysis is the most viable way, at the present stage, for studying the inside details of heat sources, mass transport and temperature distributions.

There are some valuable studies which model the tubular type solid oxide fuel cells [5–9]. One obvious weakness of these studies is that they did not make any analysis for the SOFC performance when it is working in a cell stack. Although it is likely that a SOFC might demonstrate similar performance whether it is operated as a single SOFC unit or in a cell stack, a pertinent modeling or reliable analysis for this is very important for the practical operation of a SOFC stack. The primary effort in this study will be focused on this issue.

Another weakness of the previous modeling work by other researchers is that, instead of employing a field so-

* Corresponding author. Tel.: +1-412-624-3069; fax: +1-412-624-4846.
E-mail address: pel1@pitt.edu (P.-W. Li).

0378-7753/$ – see front matter © 2003 Elsevier B.V. All rights reserved.
doi:10.1016/j.jpowsour.2003.06.001

Nomenclature

A_{cell}	area of electrolyte layer (m^2)
C_p	heat capacity (J/(kg °C))
$D_{I,m}$	mass diffusivity of gas I in gas mixture (m^2/s)
E	electromotive force (V)
F	Faraday's constant 96486.7 (C/mol)
ΔG	Gibbs free energy change (J/mol)
ΔG°	standard Gibbs free energy change (J/mol)
H	the interval from the exit of air-inducing tube to the closed end of cell (m)
ΔH	enthalpy change of the reaction (J/mol)
i	current (A)
I_{cell}	average current density based on area of electrolyte layer (mA/m^2)
L	length of fuel cell (m)
$\dot{m}$	mass flux (g/(m^2s))
M	formula weight (g/mol)
M_f	mole flow rate of fuel (mol/s)
p	pressure (Pa)
P	ratio of a pressure over 1.013×10^5 Pa; center position of a control volume or area
$\dot{q}$	volumetric heat source (W/m^3)
Q	heat generation (W)
r	radial coordinate (m)
r^a, r^c, r^e	average radius of the anode, cathode and electrolyte, respectively (m)
R	universal gas constant 8.31434 (J/(mol K))
R^a, R^c	discretized electrical resistance in the anode and cathode, respectively (Ω)
R^e	discretized ionic resistance in electrolyte layer (Ω)
ΔS	entropy change of the reaction (J/(mol K))
T	temperature (K)
u, v	velocities in axial and radial directions, respectively (m/s)
U	utilization factor for hydrogen and oxygen (%)
V^a, V^c	electrical potential at anode and cathode, respectively (V)
V_{cell}	cell terminal voltage (V)
x	coordinate in axial direction (m)
Δx	mesh size or a section in axial direction (m)
X	mole fraction (%)
$\bar{x}$, $\bar{y}$, $\bar{z}$	mole numbers of CH_4, CO and H_2 that involve in the reforming, shift and electrochemical reactions, respectively (mol/s)
Y	mass fraction (%)

Greek letters

δ^a, δ^c, δ^e	thickness of anode, cathode and electrolyte layers, respectively (m)
η^{act}	activation polarization (V)
$\Delta\theta$	mesh size in peripheral direction (°)
λ	thermal conductivity (W/(m °C))
μ	dynamic viscosity (kg/(m s))
ρ	density (kg/m^3)
ρ^e	resistivity (Ω m)

Subscripts

air	air flow
CH_4	methane
CO	carbon monoxide
CO_2	carbon dioxide
e, w, n, s	interfaces between the P-centered control-volume and its neighboring control-volumes of east, west, north and south
E, W, N, S	control-volumes that locate east, west, north and south to the P-centered control-volume
f, fuel	fuel
H_2	hydrogen
H_2O	water vapor
I	gas species
O_2	oxygen
P	center of a control-volume or -area
PR	equilibrium of reforming reaction
PS	equilibrium of shift reaction
x	axial position
Δx	axial section

Superscripts

a	anode
air	air flow
c	cathode
CH_4	methane
CO	carbon monoxide
CO_2	carbon dioxide
e	electrolyte
f, fuel	fuel
H_2	hydrogen
in	inlet of fuel or air in a concerned section
I	gas species
O_2	oxygen
out	outlet of fuel or air in a concerned section
R	reaction

lution for the flow, heat and mass transfer for obtaining the local species' mass fractions, temperatures and the electromotive forces in the fuel cell, most authors used constant heat and mass transfer coefficients based on a fully developed laminar flow approximation at constant wall temperature and mass flux. In fact, the tubular SOFC is a heat-generating tube with different flow streams on both the inner and outer side. The coupled heat and mass transfer in

the two streams are not applicable to the case of constant wall temperature/concentration or the case of constant wall flux of heat/mass. Therefore, the fully developed laminar flow approximation for Nusselt and Sherwood numbers at constant wall temperature/concentration can no longer be applied to the SOFC. There is not doubt that significant deviation might occur as has been well discussed in [10]. As has been discussed in the author's previous work [11], we will avoid the fully developed laminar flow approximation of Nusselt and Sherwood numbers at constant wall temperature/concentration in this study, instead, a complete field solution of the governing equations for the heat and mass transfer in the entire domain of a SOFC working in a cell stack will be employed.

2. Model development

2.1. Delineation of the domain pertain to a single SOFC in a cell stack

Fig. 1 shows the schematic view of a typical tubular SOFC. The layers of cathode, electrolyte and anode are laminated onto the gas diffusible porous support tube. The cell tube is fabricated in the structure like a test tube so that air is supplied through a concentric air-inducing tube inserted inside the tubular cell from its open-end. Oxygen in air is ionized at the cathode (air electrode), and the oxide ions produced are conducted through the electrolyte to the anode (fuel electrode). Oxidization of the fuel (hydrogen or carbon monoxide) that diffuses from the core region of the fuel stream occurs at the anode. In the meantime, the products from the chemical/electrochemical reactions diffuse back into the fuel stream and are removed together with the remaining unreacted fuel.

In a practical tubular SOFC stack, many tubular cells are mounted in a container in a cell bundle, as shown in Fig. 2. For most of the tubular cells mounted in the bundle, each of them is surrounded by four others. Therefore, it is possible, and very likely, that most of the single tubular SOFCs work under the same environment of temperature and concentrations of gas species. This allows us to define a controllable

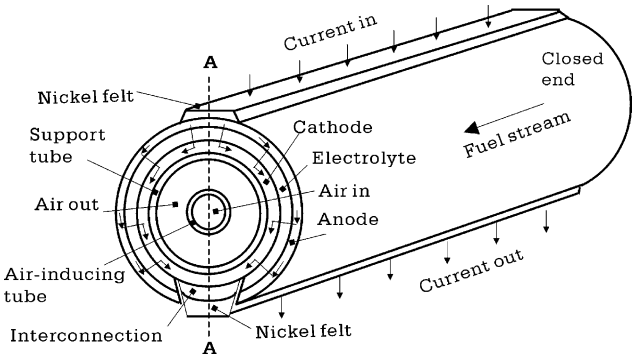

Fig. 1. Schematic of a tubular solid oxide fuel cell (SOFC).

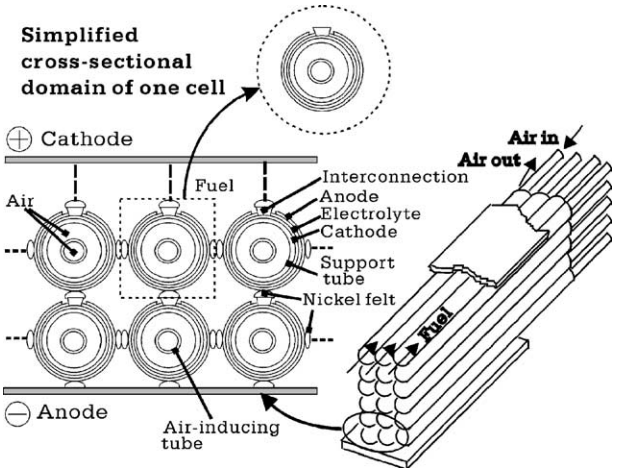

Fig. 2. Orientation of a tubular SOFC in a cell stack.

domain in the cross-section, which pertains to one particular single cell, as outlined by the dashed-line square in Fig. 2. There must be no flow velocity and fluxes of heat and mass across the outline. This will significantly simplify the analysis of a cell stack. In other words, through analysis of the heat/mass transfer and the chemical/electrochemical performance of one single cell and its controllable area, one can obtain results that are very useful for evaluating the performance of a cell stack.

With the longitudinal direction also being considered, the heat and mass transfer in the above outlined square area enclosing the tubular SOFC are in three dimensions. For a solution of the three-dimensional governing equations of momentum, energy and species conservation, a large number of discretized mesh is necessary and that will make the computation too difficult to be conducted with a personal computer. In order to reduce computation cost, the square area enclosing the tubular SOFC is approximated to be an equivalent circular area and therefore, the domain enclosing the interested single tubular SOFC is viewed as a two-dimensional axial-symmetric one, as seen in Fig. 2. However, the zero flux or insulation of heat and mass transfer at the boundary remains unchanged even though this geometric approximation is applied.

2.2. Electrochemical/chemical reactions and electromotive force

If the SOFC operates based on pre-reformed natural gas [12], the fuel stream might have components of CH_4, CO, CO_2, H_2, and H_2O. Then, the reforming and shift reactions will occur along with the electrochemical reaction, i.e. the oxidization of hydrogen

$$CH_4 + H_2O \leftrightarrow CO + 3H_2 \quad \text{(reforming)} \tag{1}$$

$$CO + H_2O \leftrightarrow CO_2 + H_2 \quad \text{(shift)} \tag{2}$$

$$H_2 + \tfrac{1}{2}O_2 \leftrightarrow H_2O \quad \text{(electrochemical oxidation)} \tag{3}$$

In fact, the oxidization of CO also occurs at the anode. However, the variation of CH_4, CO, CO_2, H_2 and H_2O must satisfy the chemical reaction equilibrium of Eqs. (1) and (2), therefore, there is no necessity to distinguish whether the electrochemical reaction step involves oxidation of H_2 or CO because both the oxidation of H_2 and CO yield the same electromotive force [2].

$$E = \frac{-\Delta G}{2F} = \frac{-\Delta G^\circ}{2F} + \frac{RT}{2F}\ln\left(\frac{P_{H_2}P_{O_2}^{0.5}}{P_{H_2O}}\right) \quad (4)$$

where ΔG° is the variation of standard state (1.013×10^5 Pa) Gibbs' free energy of the reaction of Eq. (3), P_{H_2} and P_{H_2O} are the ratios of partial pressure over the standard state pressure of 1.013×10^5 Pa for hydrogen and water vapor at the electrolyte/anode interface, respectively, and P_{O_2} is that for oxygen at the electrolyte/cathode interface.

In the electrochemical reaction proceeding at temperature, T, the changes of chemical enthalpy, ΔH, entropy, ΔS and Gibb's free energy, ΔG, have the thermodynamic relationship:

$$\Delta G = \Delta H - T\Delta S \quad (5)$$

Theoretically, $-\Delta G$ is converted into electrical power as was given in Eq. (4), while $-T\Delta S$ is released in the form of thermal energy during the electrochemical reaction. Along with the consumption and production of the gas species in fuel and air flows, the mass fractions of the reactants and products from the electrochemical/chemical reactions also vary in the flow streams of fuel and air. This yields the localized electromotive force, E, over the electrolyte layer, which yields the localized ion/charge transfer rate through the electrolyte layer

$$i = \frac{E - \eta^{act} - (V^c - V^a)}{R^e} \quad (6)$$

where V^a and V^c are the potentials in anode and cathode, respectively, η^{act} is the over-potential incurred by the activation polarization [13] which occurs at both anode and cathode,

$$\eta^{act} = \frac{2RT}{n_e F}\sinh^{-1}\left(\frac{\bar{i}}{2\bar{i}_0}\right) \quad (7)$$

where n_e is electrons transferred per reaction (for the reaction of Eq. (3), it is 2), $\bar{i}$ is the current density across electrolyte and, $\bar{i}_0$ is the exchange current density which is 5300 A/m^2 for anode and 2000 A/m^2 for cathode. The R^e in Eq. (6) is the ionic resistance of the electrolyte layer in the thickness of δ^e and a unit area of ΔA, which is in the form of

$$R^e = \rho^e\frac{\delta^e}{\Delta A} \quad (8)$$

where the ρ^e is the ionic resistivity of electrolyte, which is a strong function of temperature [14,15] as given in Table 1.

In a tubular type SOFC, the current is circumferentially collected to the nickel felt. The ohmic loss in the circumferential pathway is significant and certainly not negligible. In this work, we apply a network circuit, as shown in Fig. 3, to the three layers of anode, electrolyte and cathode to analyze the current, or charge transfer rate. Because the current collection is symmetric in the peripheral direction in the cell tube, only one-half tube is deployed (over 14 nodes in peripheral direction) in the analysis. Applying Kirchhoff's law of current, we obtain the equation associating the potentials of the interested grid P with the potentials of its neighboring points, east, west, north, south and the corresponding grid P in the cathode

$$\left(\frac{V_E^a - V_P^a}{R_e^a} + \frac{V_W^a - V_P^a}{R_w^a}\right) + \left(\frac{V_N^a - V_P^a}{R_n^a} + \frac{V_S^a - V_P^a}{R_s^a}\right) + \left[\frac{V_P^c - V_P^a - (E_P - \eta_P^{act})}{R_P^e}\right] = 0 \quad (9)$$

In the same way for a grid P in the cathode, there is

$$\left(\frac{V_E^c - V_P^c}{R_e^c} + \frac{V_W^c - V_P^c}{R_w^c}\right) + \left(\frac{V_N^c - V_P^c}{R_n^c} + \frac{V_S^c - V_P^c}{R_s^c}\right) + \left[\frac{V_P^a - V_P^c + (E_P - \eta_P^{act})}{R_P^e}\right] = 0 \quad (10)$$

where R^a and R^c are the discretized resistance in anode and cathode, respectively, which are determined according to the resistivity, the length of current path and the area the current acted on. The material resistivities of both cathode and anode are also given in Table 1, as the function of temperature.

With all the equations for the discretized grids in both cathode and anode enclosed, a matrix represented by the pair of Eqs. (9) and (10) is formatted. For the solution of such

Table 1
Properties of fuel cell components

	Thermal conductivity (W/(m K))	Electric or ionic resistivity (Ω cm)
Cathode	6.0	$0.008114\exp(500/T)$
Electrolyte	2.7	$10.0\exp[10092(1.0/T - 1.0/1273.15)]$
Anode	11.0	$0.00298\exp(-1392/T)$
Support tube	1.1	–
Air-inducing tube	1.1	–

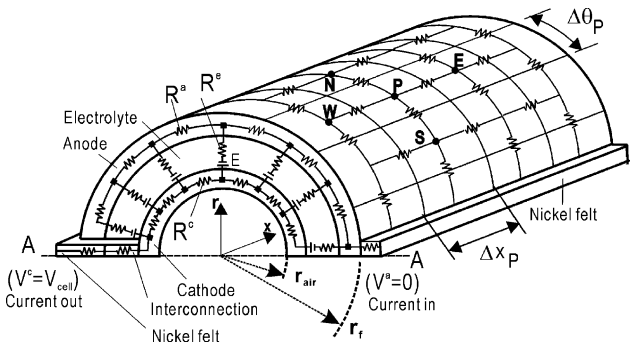

Fig. 3. Allocation of nodes for computation of electric potentials in electrodes.

a matrix equation for potentials, the following approximations are useful: (1) at the two ends of the cell tube, there is no longitudinal current and, therefore, insulation condition is applicable; (2) at the symmetric plane *A–A* as shown in Figs. 1 and 3, there is no peripheral current in the cathode or anode, unless the cathode or anode is in contact with nickel felt, through which the current flows in or out; (3) the potentials on the nickel felts are assumed uniform due to their high electrical conductivities; (4) since the potential difference between the two nickel felts is the cell terminal voltage, the potential at the nickel felt in contact to the anode layer can be assumed to be zero, thus the potential at the nickel felt in contact with the cathode will be the terminal voltage of the fuel cell. Once we obtained all the local electromotive forces from Eq. (4), the only unknown condition for the matrix equation is either the total current flowing out from the cell or the potential at the nickel felt in contact with the cathode. This provides two approaches for the numerical simulation of the fuel cell. In case the total current taken from the cell is prescribed as the initial condition, the terminal voltage will be predicted as the simulation result. On the other hand, one can prescribe the terminal voltage and target the simulation computation in obtaining the total current, i.e. the summation of local current i across the entire electrolyte layer. In the present work, the first approach was adopted.

With the potentials being obtained in an electrode layer, the Joule heating in that electrode in an interested area, controlled by P, will be

$$\dot{q}_{\mathrm{P}}^{\mathrm{a}} = \frac{1}{2}\left[\frac{(V_{\mathrm{E}}^{\mathrm{a}} - V_{\mathrm{P}}^{\mathrm{a}})^2}{R_{\mathrm{e}}^{\mathrm{a}}} + \frac{(V_{\mathrm{W}}^{\mathrm{a}} - V_{\mathrm{P}}^{\mathrm{a}})^2}{R_{\mathrm{w}}^{\mathrm{a}}} + \frac{(V_{\mathrm{N}}^{\mathrm{a}} - V_{\mathrm{P}}^{\mathrm{a}})^2}{R_{\mathrm{n}}^{\mathrm{a}}} + \frac{(V_{\mathrm{S}}^{\mathrm{a}} - V_{\mathrm{P}}^{\mathrm{a}})^2}{R_{\mathrm{s}}^{\mathrm{a}}}\right](\Delta x_{\mathrm{P}} r^{\mathrm{a}} \Delta\theta_{\mathrm{P}} \delta^{\mathrm{a}})^{-1} \tag{11}$$

$$\dot{q}_{\mathrm{P}}^{\mathrm{c}} = \frac{1}{2}\left[\frac{(V_{\mathrm{E}}^{\mathrm{c}} - V_{\mathrm{P}}^{\mathrm{c}})^2}{R_{\mathrm{e}}^{\mathrm{c}}} + \frac{(V_{\mathrm{W}}^{\mathrm{c}} - V_{\mathrm{P}}^{\mathrm{c}})^2}{R_{\mathrm{w}}^{\mathrm{c}}} + \frac{(V_{\mathrm{N}}^{\mathrm{c}} - V_{\mathrm{P}}^{\mathrm{c}})^2}{R_{\mathrm{n}}^{\mathrm{c}}} + \frac{(V_{\mathrm{S}}^{\mathrm{c}} - V_{\mathrm{P}}^{\mathrm{c}})^2}{R_{\mathrm{s}}^{\mathrm{c}}}\right](\Delta x_{\mathrm{P}} r^{\mathrm{c}} \Delta\theta_{\mathrm{P}} \delta^{\mathrm{c}})^{-1} \tag{12}$$

$$\dot{q}_{\mathrm{P}}^{\mathrm{e}} = \left[\frac{(E_{\mathrm{P}} - \eta_{\mathrm{P}}^{\mathrm{act}} - V_{\mathrm{P}}^{\mathrm{c}} + V_{\mathrm{P}}^{\mathrm{a}})^2}{R_{\mathrm{P}}^{\mathrm{e}}}\right](\Delta x_{\mathrm{P}} r^{\mathrm{e}} \Delta\theta_{\mathrm{P}} \delta^{\mathrm{e}})^{-1} \tag{13}$$

where the r and δ with corresponding superscripts a, c and e are the average radius and thickness, respectively, for the anode, cathode and electrolyte, and Δx_{P} and $\Delta\theta_{\mathrm{P}}$ are the P-controlled mesh size in axial and peripheral directions as shown in Fig. 3. The heating rate induced from activation polarization in anode and cathode is in the form of:

$$\dot{q}_{\mathrm{P}}^{\mathrm{act,a}} = \frac{i_{\mathrm{P}} \eta_{\mathrm{P}}^{\mathrm{act,a}}}{\Delta x_{\mathrm{P}} r^{\mathrm{a}} \Delta\theta_{\mathrm{P}} \delta^{\mathrm{a}}} \tag{14}$$

$$\dot{q}_{\mathrm{P}}^{\mathrm{act,c}} = \frac{i_{\mathrm{P}} \eta_{\mathrm{P}}^{\mathrm{act,c}}}{\Delta x_{\mathrm{P}} r^{\mathrm{c}} \Delta\theta_{\mathrm{P}} \delta^{\mathrm{c}}} \tag{15}$$

The thermodynamic heat generation occurring at the anode/electrolyte interface in the interested area, controlled by P, is:

$$Q_{\mathrm{P}}^{\mathrm{R}} = \frac{(\Delta H - \Delta G) i_{\mathrm{P}}}{2F} \tag{16}$$

The current i_{P} and heating rates distribute non-uniformly along the axial and peripheral directions. Because two-dimensional flow and heat/mass transfer are assumed, the peripheral average of the local heating rates and ionic conducting rate or current across the electrolyte is introduced into the axial-symmetric equations governing the conservation of momentum, heat and mass.

If the SOFC operates based on pre-reformed natural gas, the variation of CH_4, CO, CO_2, H_2, and H_2O associate each other and need to be determined based on the condition of chemical reaction equilibrium. For convenience of analysis, the mole numbers of CH_4, CO and H_2 reacted in reactions by Eqs. (1)–(3) in a concerned section in fuel channel are represented by $\bar{x}$, $\bar{y}$ and $\bar{z}$, respectively. Then, the variation of mole numbers of all the species in an interested section of fuel channel from its inlet to outlet is:

$$\mathrm{CH}_4^{\mathrm{out}} = \mathrm{CH}_4^{\mathrm{in}} - \bar{x} \tag{17}$$

$$\mathrm{CO}^{\mathrm{out}} = \mathrm{CO}^{\mathrm{in}} + \bar{x} - \bar{y} \tag{18}$$

$$\mathrm{CO}_2^{\mathrm{out}} = \mathrm{CO}_2^{\mathrm{in}} + \bar{y} \tag{19}$$

$$\mathrm{H}_2^{\mathrm{out}} = \mathrm{H}_2^{\mathrm{in}} + 3\bar{x} + \bar{y} - \bar{z} \tag{20}$$

$$\mathrm{H}_2\mathrm{O}^{\mathrm{out}} = \mathrm{H}_2\mathrm{O}^{\mathrm{in}} - \bar{x} - \bar{y} + \bar{z} \tag{21}$$

The variation of the total mole numbers of the fuel flow from inlet to outlet of the interested section becomes:

$$M_{\mathrm{f}}^{\mathrm{out}} = M_{\mathrm{f}}^{\mathrm{in}} + 2\bar{x} \tag{22}$$

According to the chemical equilibrium, the equilibrium constants of the reaction by Eqs. (1) and (2) are in the forms of

$$K_{\mathrm{PR}} = \frac{P_{\mathrm{H_2}}^3 P_{\mathrm{CO}}}{P_{\mathrm{CH_4}} P_{\mathrm{H_2O}}} = \exp\left(-\frac{\Delta G^{\circ}_{\mathrm{reforming}}}{RT}\right) \tag{23}$$

$$K_{\mathrm{PS}} = \frac{P_{\mathrm{CO_2}} P_{\mathrm{H_2}}}{P_{\mathrm{CO}} P_{\mathrm{H_2O}}} = \exp\left(-\frac{\Delta G^{\circ}_{\mathrm{shift}}}{RT}\right) \tag{24}$$

where $P_{\mathrm{H_2O}}$, $P_{\mathrm{H_2}}$, $P_{\mathrm{CH_4}}$, P_{CO} and $P_{\mathrm{CO_2}}$ are the ratios of the partial pressure over the standard state pressure of 1.013×10^5 Pa for the corresponding species in fuel stream of the interested section. When expressing the partial pressures in terms of the species' corresponding mole numbers and the overall pressure, the equilibrium constants is in the form of

$$K_{\mathrm{PR}} = \frac{[(\mathrm{CO}^{\mathrm{in}} + \bar{x} - \bar{y})/(M_{\mathrm{f}}^{\mathrm{in}} + 2\bar{x})] \times [(\mathrm{H}_2^{\mathrm{in}} + 3\bar{x} + \bar{y} - \bar{z})/(M_{\mathrm{f}}^{\mathrm{in}} + 2\bar{x})]^3 P^2}{[(\mathrm{CH}_4^{\mathrm{in}} - \bar{x})/(M_{\mathrm{f}}^{\mathrm{in}} + 2\bar{x})] \times [(\mathrm{H_2O}^{\mathrm{in}} - \bar{x} - \bar{y} + \bar{z})/(M_{\mathrm{f}}^{\mathrm{in}} + 2\bar{x})]} \tag{25}$$

$$K_{PS} = \frac{[(H_2^{in} + 3\bar{x} + \bar{y} - \bar{z})/(M_f^{in} + 2\bar{x})] \times [(CO_2^{in} + \bar{y})/(M_f^{in} + 2\bar{x})]}{[(CO^{in} + \bar{x} - \bar{y})/(M_f^{in} + 2\bar{x})] \times [(H_2O^{in} - \bar{x} - \bar{y} + \bar{z})/(M_f^{in} + 2\bar{x})]} \quad (26)$$

where P is the ratio of overall pressure over the standard state pressure of 1.013×10^5 Pa for a particular section in the fuel stream.

In a particular section, the reacted H_2 and O_2 are related to the current transfer rate across the electrolyte layer of the section, which is obtainable through the solution of the network circuit as discussed in the preceding paragraphs.

$$\bar{z} = \frac{i}{2F} \quad (27)$$

$$\bar{z}^{O_2} = \frac{i}{4F} \quad (28)$$

With the $\bar{z}$ and the temperature of gas species available, the $\bar{x}$ and $\bar{y}$ are obtainable from Eqs. (25) and (26). The reforming and shift reactions take place at the anode, which serves as the catalyst. Therefore, the species' variations are considered as mass fluxes going inward or outward from the anode surface. Mass fluxes of CO, CO_2, CH_4, H_2O on anode/fuel interface in a Δx section at position x are thus in the form of:

$$\dot{m}_x^{H_2} = M_{H_2} \frac{1}{2\pi r_f \Delta x} (3\bar{x}_{\Delta x} + \bar{y}_{\Delta x} - \bar{z}_{\Delta x}) \quad (29)$$

$$\dot{m}_x^{CO} = M_{CO} \frac{1}{2\pi r_f \Delta x} (\bar{x}_{\Delta x} - \bar{y}_{\Delta x}) \quad (30)$$

$$\dot{m}_x^{CO_2} = M_{CO_2} \frac{1}{2\pi r_f \Delta x} \bar{y}_{\Delta x} \quad (31)$$

$$\dot{m}_x^{H_2O} = M_{H_2O} \frac{1}{2\pi r_f \Delta x} (\bar{z}_{\Delta x} - \bar{x}_{\Delta x} - \bar{y}_{\Delta x}) \quad (32)$$

$$\dot{m}_x^{CH_4} = M_{CH_4} \frac{1}{2\pi r_f \Delta x} (-\bar{x}_{\Delta x}) \quad (33)$$

In a Δx section at position, x, the mass flux of O_2 on cathode/air interface towards the electrolyte is:

$$\dot{m}_x^{O_2} = M_{O_2} \frac{1}{2\pi r_{air} \Delta x} (\bar{z}_{\Delta x}^{O_2}) \quad (34)$$

With the reacted mole numbers of CH_4 and CO determined, the heat released from reforming and shift reaction is thus in the forms of:

$$Q_{\Delta x}^{reforming} = \Delta H^{reforming} \bar{x}_{\Delta x} \quad (35)$$

$$Q_{\Delta x}^{shift} = \Delta H^{shift} \bar{y}_{\Delta x} \quad (36)$$

2.3. Flow and heat/mass transfer

From the preceding discussions, an axial-symmetrical two-dimensional (x–r) computation domain is profiled as shown in Fig. 4, which includes two flow streams and solid area that locates the cell tube and air-inducing tube. The following governing equations, Eqs. (37)–(40), for momentum, energy and species transport are applicable universally to the entire computation domain, however, zero velocities need to be assigned to solid area in the numerical treatment. As the species fractions vary in the flow field, all thermal and transport properties in these equations are localized by taking into consideration of the local species' concentration, temperature and pressure [16,17]. This is a specific point for the flow, heat and mass transfer governing equations in fuel cells.

$$\frac{\partial(\rho u)}{\partial x} + \frac{1}{r}\frac{\partial(r\rho v)}{\partial r} = 0 \quad (37)$$

$$\frac{\partial(\rho uu)}{\partial x} + \frac{1}{r}\frac{\partial(r\rho vu)}{\partial r} = -\frac{\partial p}{\partial x} + \frac{\partial}{\partial x}\left(\mu\frac{\partial u}{\partial x}\right) + \frac{1}{r}\frac{\partial}{\partial r}\left(r\mu\frac{\partial u}{\partial r}\right) + \frac{\partial}{\partial x}\left(\mu\frac{\partial u}{\partial x}\right) + \frac{1}{r}\frac{\partial}{\partial r}\left(r\mu\frac{\partial v}{\partial x}\right) \quad (38)$$

$$\frac{\partial(\rho uv)}{\partial x} + \frac{1}{r}\frac{\partial(r\rho vv)}{\partial r} = -\frac{\partial p}{\partial r} + \frac{\partial}{\partial x}\left(\mu\frac{\partial v}{\partial x}\right) + \frac{1}{r}\frac{\partial}{\partial r}\left(r\mu\frac{\partial v}{\partial r}\right) + \frac{\partial}{\partial x}\left(\mu\frac{\partial u}{\partial r}\right) + \frac{1}{r}\frac{\partial}{\partial r}\left(r\mu\frac{\partial v}{\partial r}\right) - \frac{2\mu v}{r^2} \quad (39)$$

$$\frac{\partial(\rho C_p uT)}{\partial x} + \frac{1}{r}\frac{\partial(r\rho C_p vT)}{\partial r} = \frac{\partial}{\partial x}\left(\lambda\frac{\partial T}{\partial x}\right) + \frac{1}{r}\frac{\partial}{\partial r}\left(r\lambda\frac{\partial T}{\partial r}\right) + \dot{q} \quad (40)$$

$$\frac{\partial(\rho uY_I)}{\partial x} + \frac{1}{r}\frac{\partial(r\rho vY_I)}{\partial r} = \frac{\partial}{\partial x}\left(\rho D_{I,m}\frac{\partial Y_I}{\partial x}\right) + \frac{1}{r}\frac{\partial}{\partial r}\left(r\rho D_{I,m}\frac{\partial Y_I}{\partial r}\right) + S_m \quad (41)$$

A mesh system of at least 66 in the r-direction and 602 in the x-direction is deployed for the computation domain. Then, all the above equations are discretized by using the finite volume approach and the SIMPLE algorithm was adopted to treat the coupling of the velocity and pressure fields [18,19].

The energy equation applied to the solid components of the cell reduces to a heat conduction equation since zero velocity is assigned there. Heat generation rates are introduced into the source term of Eq. (40). The heat conductivity for cell materials is given in Table 1. The temperature between the cell tube and the air-inducing tube might be high enough and, radiation heat exchange might exist. Numerical treatment for this radiation heat exchange is based on the method introduced in the literature [20].

The boundary conditions for the momentum, heat and mass conservation equations are as follows. On the symmetrical axis, or at $r = 0$: $v = 0$ and $\partial\phi/\partial r = 0$, where ϕ represents general variables except v. At the outmost boundary of

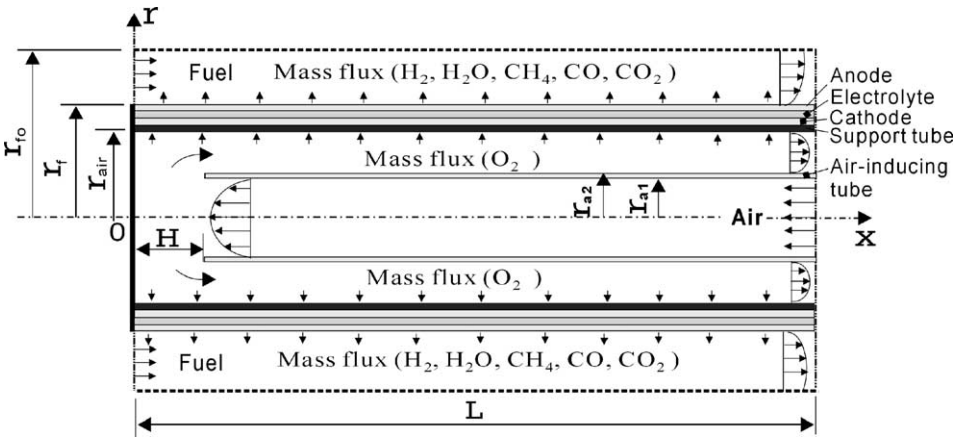

Fig. 4. Computational domain pertain to one SOFC outlined from a cell stack.

$r = r_{fo}$: thermally adiabatic conditions, impermeability for species and non-chemical reaction were assumed, that gives, $v = 0$ and $\partial\phi/\partial r = 0$, where ϕ represents general variables except v. At $x = 0$: the fuel inlet has prescribed uniform velocity, temperature and species mass fraction, and the solid part has $u = 0$, $v = 0$, $\partial T/\partial x = 0$ and $\partial Y_I/\partial x = 0$. At $x = L$: the air inlet has prescribed uniform velocity, temperature and species mass fraction; the gas exit part has $v = 0$, $\partial u/\partial x = 0$, $\partial T/\partial x = 0$ and $\partial Y_I/\partial x = 0$, and all the tube end solid part has $u = 0$, $v = 0$, $\partial T/\partial x = 0$ and $\partial Y_I/\partial x = 0$.

At the interfaces of air/support tube, $r = r_{air}$, and fuel/anode, $r = r_f$, $u = 0$ is assumed. However, in the fuel flow passage, the mass flow rate increases along the x-direction due to the transferring-in of oxide ions. Similarly, reduction of air flow rate occurs in the air flow passage, due to the ionizing of oxygen and ion-transference to the fuel side. Therefore, a radial velocity exists at $r = r_{air}$ and $r = r_f$:

$$v_f = \frac{\sum \dot{m}_x^{fuel,species}}{\rho_x^{fuel}}\Big|_{r=r_f}, \qquad v_{air} = \frac{\sum \dot{m}_x^{air,species}}{\rho_x^{air}}\Big|_{r=r_{air}} \tag{42}$$

The mass fraction at the boundaries of $r = r_{air}$ and $r = r_f$ of all participating chemical components are calculated with consideration of both diffusion and convection effects [21]:

$$\dot{m}_x^{I,air} = -D_{I,air}\rho_x^{air}\frac{\partial Y_I}{\partial r} + \rho_x^{air} Y_I v_{air} \tag{43}$$

$$\dot{m}_x^{I,fuel} = -D_{I,fuel}\rho_x^{fuel}\frac{\partial Y_I}{\partial r} + \rho_x^{fuel} Y_I v_f \tag{44}$$

It is worth mentioning that the mass/mole fraction obtained from this calculation will be used for the determination of the partial pressures and thus the local electromotive forces with Eq. (4).

2.4. Profile of the overall simulation scheme for a tubular SOFC

The species' mole compositions, temperature and flow rates of fuel and air are the basic prescribed conditions for a fuel cell operation. In addition, the cell terminal voltage is another decisive condition to designate a fuel cell operating condition. Other resultant parameters for a fuel cell will follow these conditions. In the same style, a numerical simulation can also follow these prescribed conditions to predict the output current and all the other internal details, for example, the local temperature, mass fractions, percentage of utilized fuel, oxygen, etc. However, instead of the cell terminal voltage, one can also prescribe the output current, together with the basic prescribed conditions, to designate a fuel cell operating condition. In such a case, following the prescribed conditions, the cell terminal voltage and other details will be predicted. This is the scheme used in this study.

It is quite common in practice that the output current is prescribed in terms of the average current density of the fuel cell. Also, instead of the flow rates of fuel and air, the stoichiometric data are prescribed in terms of the utilization percentage of hydrogen and oxygen. This kind of designation of the operating conditions gives the convenience for comparing the fuel cell performance based on the same level of average current density and the hydrogen and oxygen utilization percentage. The inlet velocities of fuel and air are, then, obtainable in the forms of:

$$u_{fuel} = \left(\frac{A_{cell} I_{cell}}{2F U_{H_2} X_{H_2} A_{fuel}}\right)\frac{RT_f}{P_f} \tag{45}$$

$$u_{air} = \left(\frac{A_{cell} I_{cell}}{4F U_{O_2} X_{O_2} A_{air}}\right)\frac{RT_{air}}{P_{air}} \tag{46}$$

where A_{fuel} and A_{air} are the cross-sectional inlet areas of the fuel and air; P_f, P_{air} and T_f, T_{air} are the inlet pressures and temperature of the fuel and air flows, respectively; X_{H_2} and X_{O_2} are the mole fractions of hydrogen in the fuel and oxygen in the air, respectively.

The computation process is highly iterative and interdigitated in nature. As the first step, the local temperature, pressure, species' mass fraction are used in the network circuit analysis to obtain the cell terminal voltage, local current across the electrolyte and thus the local species' transfer fluxes and heating rates. In the second step, the local temperature, pressure and species' mass fractions are, in turn, obtained through solution of the governing equations under new internal and boundary conditions determined by the latest-available species' flux and heating rate. The two steps iterate interactively until convergence is obtained.

3. Results and discussion for validation computation

Experimental data and operating conditions for tubular SOFCs from different papers, respectively, by Hagiwara et al. [22], Hirano et al. [7], Singhal [23,24] and Tomlins and Jaszar [25] have been referred for the validation of the present numerical model. The fuel used by Hirano et al. [7] had components of H_2, H_2O, CO and CO_2. Thus, there is a water-shift of the carbon monoxide in the fuel cell to be considered. The fuel used by other researchers [22–25] had components of H_2 and H_2O and there is only the electrochemical reaction to be considered. The dimensions of the three different solid oxide fuel cells tested in their studies are listed in Table 2, in which the mesh size adopted in our numerical computation is also given. Correspondingly, Table 3 lists the species mole fraction and temperature of fuel and air in their test, which are the prescribed conditions in this computation. The experimental data for these SOFCs in different structural dimensions and operating conditions is expected to facilitate a wide benchmark for validation of the numerical model presented in this study.

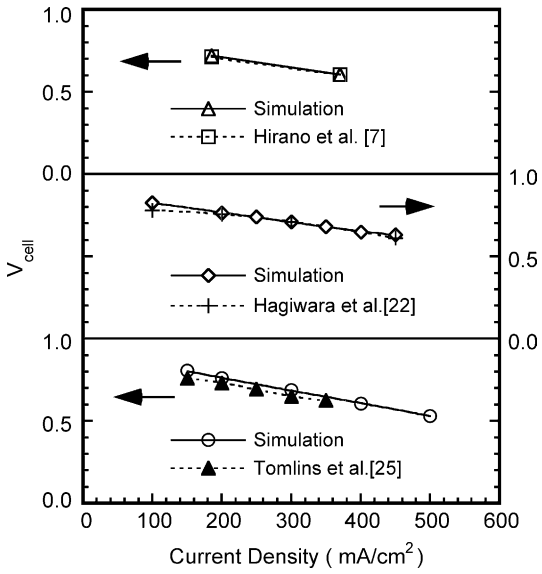

Fig. 5. Prediction and testing results of cell voltage vs. current density. (Operating pressure of the cell tested by Hagiwara et al. [22] and Hirano et al. [7] are 1.013×10^5 Pa, and that by Tomlins and Jaszar [25] is 5.065×10^5 Pa).

3.1. The SOFC terminal voltage versus current density for different cells

Fig. 5 shows the numerically predicted cell terminal voltage and the experimental data in the literature at different cell current densities. The relative deviation between the

Table 2
Dimensions of the cited SOFCs and mesh size used in this computation

	Data sequence: outer diameter (mm)/thickness (mm)/length (mm)		
	[22]	[7]	[23–25]
Air-inducing tube	7.00/1.00/485	6.00/1.00/290	12.00/1.00/1450
Support tube	–	13.00/1.50/300	–
Cathode	15.72/2.20/500	14.40/0.70/300	21.72/2.20/1500
Electrolyte	15.80/0.04/500	14.48/0.04/300	21.80/0.04/1500
Anode	16.00/0.10/500	14.68/0.10/300	22.00/0.10/1500
Fuel boundary	18.10/–/500	16.61/–/300	24.87/–/1500
Grid number ($r \times x$)	66 × 602	66 × 602	66 × 1602

Table 3
Species' mole fraction, utilization percentage and temperature

	Air [O_2 (%)–U_{O_2}/N_2 (%)/T (°C)]	Fuel [H_2 (%)–U_{H_2}/H_2O (%)/CH_4 (%)/CO (%)/CO_2 (%)/T (°C)]
[22]	21.00–17.00/79.00/600.0	98.64–85.00/1.36/0/0/0/900.0
[7]	21.00–25.00/79.00/600.0[a]	55.70–80.00/27.70/0/10.80/5.80/800.0
	21.00–25.00/79.00/400.0[b]	55.70–80.00/27.70/0/10.80/5.80/800.0
[24,25]	21.00–17.00/79.00/600.0	98.64–85.00/1.36/0/0/0/800.0

[a] Case of current density = 185 mA/cm^2.
[b] Case of current density = 370 mA/cm^2.

model-predicted cell voltages and the experimental data is no larger than 1.0% for the cell tested by Hirano et al. [7], 5.6% for that by Hagiwara et al. [22], and 6.0% for that by Tomlins and Jaszar [25]. Such a good agreement for the terminal voltages between the model-prediction and the experiment from different researchers is a strong demonstration that the present numerical model is quite reliable.

A comparison of the fuel cell performance in terms of the cell voltage versus the cell current density for the simulated results of the three SOFCs in different diameter and length may be necessary. It is found from Fig. 5 that, under the same cell current density, the cell voltage of the SOFC tested by Hagiwara et al. [22] is the highest and that by Hirano et al. [7] is the lowest. The mole fraction of hydrogen is low in the fuel for the SOFC tested by Hirano et al. [7], which might be the major reason that it has the lowest cell voltage. Because the current must be collected circumferentially in a tubular type fuel cell, the large diameter of cell tube by Singhal [24] and Tomlins and Jaszar [25] will lead to a longer current pathway and thus their cell voltage is lower than that by Hagiwara et al. [22] even though the data shown in Fig. 5 was at a pressurized operation of 5.065×10^5 Pa, which, in fact, helps to improve the cell voltage.

Under a constant current density of 300 mA/cm^2, the cell voltage and power increase with the increasing operating pressure, as seen in Fig. 6. The agreement between our simulation results and the experimental data by Singhal [24] is

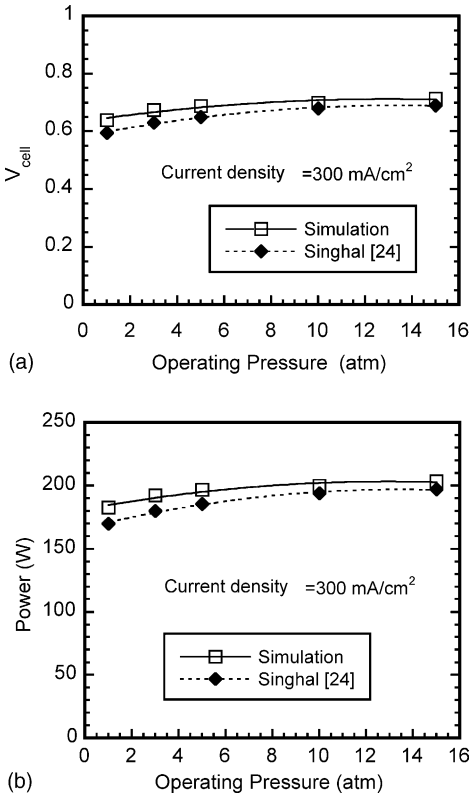

Fig. 6. Prediction and testing results of the cell voltage and power vs. operating pressure. (Experimental data was from Singhal [24] under cell current density of 300 mA/cm^2.)

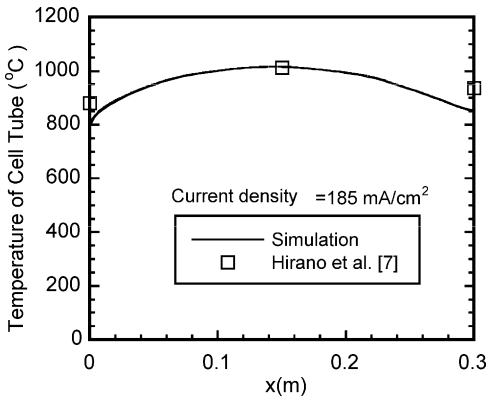

Fig. 7. Cell temperature distribution from prediction and experimental testing. (Experimental data are from Hirano et al. [7] at cell current density of 185 mA/cm^2.)

quite good, showing a maximum deviation of 7.4% at low operating pressures. When the operating pressure increases from 1.013×10^5 to 5.065×10^5 Pa, the cell output power shows a significant improvement of 9%. However, raising the operating pressure becomes less effective for improving the output power when the operating pressure is high, for example, the cell output power has only a 6% increase when the operating pressure increases from 5.065×10^5 to 1.520×10^6 Pa. This is because that the operating pressure contributes to the cell voltage in a logarithmic manner. Nevertheless, the cell output power can be improved significantly by pressurized operation. Increasing the operating pressure from 1.013×10^5 to 1.520×10^6 Pa, the cell output power can have an increment of 15.8%.

3.2. Results of the cell temperature distribution

Because the measurement of temperature in a SOFC is very difficult, only three experimental data, the temperature at two ends and in the middle of the cell tube, was available from the work by Hirano at al. [7]. Shown in Fig. 7 is the simulated cell temperature distribution for the SOFC tested by Hirano et al. [7]. The agreement of the simulated data and the experimental results is rather good in the middle, where the hotspot locates, and relatively larger deviation appears at the two ends of the cell. For further comparison, more experimental data tested for different SOFCs is expected in the future.

The predicted temperature distribution for the fuel cells tested by Hagiwara et al. [22], and Tomlins and Jaszar [25] is given in Fig. 8. Generally, the two ends of the cell tube have a lower temperature than the middle of the cell tube. However, at low current densities, the hotspot is located closer to the closed end of the cell. With increasing current density, the hotspot shifts to the open-end side and its temperature also decreases, which makes the uniformity of temperature distribution along the fuel cell better. The heat transfer between the cooling air and the cell tube at the cell closed-end region is like a jet impingement heat transfer, although the

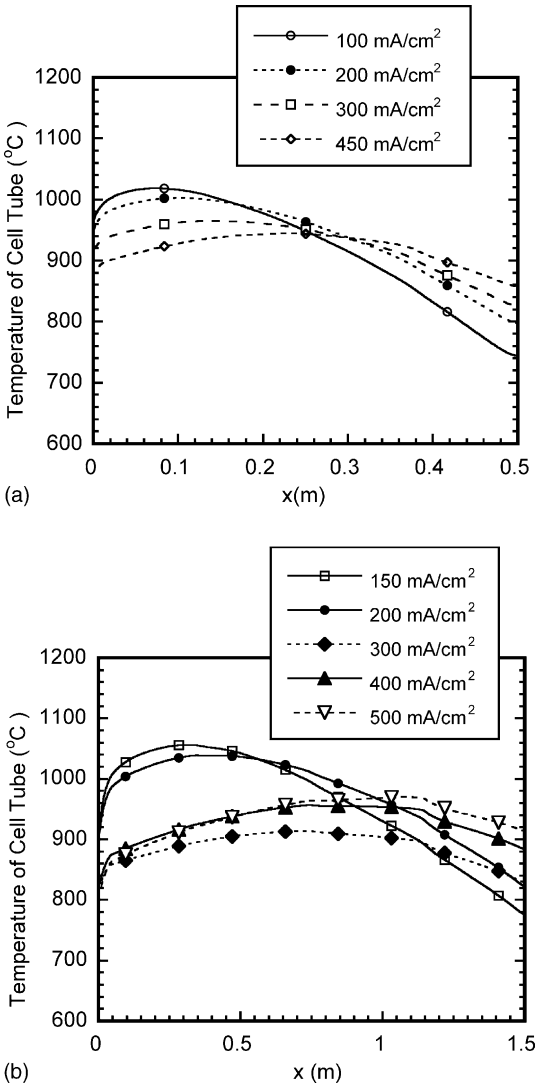

Fig. 8. Predicted cell tube temperature distribution under different current density: (a) the cell tested by Hagiwara et al. [22]; (b) the cell tested by Singhal [24] and Tomlins and Jaszar [25].

exit velocity from the air-inducing tube is quite low. Therefore, the velocity of the exit air from the air-inducing tube affects the heat transfer coefficient significantly. For the high current density case, the air flow rate becomes larger accordingly, thus the heat transfer coefficient between the air and the fuel cell closed-end region is increased. This can prohibit the temperature level of the closed-end region of the fuel cell significantly. Since the air receives much heat at the closed-end region, its cooling for the fuel cell in the downstream region becomes weak and thus, the uniformity of cell temperature distribution becomes much better when at high current densities.

3.3. Details of flow, temperature and concentration fields

Fig. 9 shows the flow and temperature fields for the SOFC tested by Hirano et al. [7] at a current density of 185 mA/cm^2. The air speed in the air-inducing tube has a slight acceleration because the air absorbs heat and expands in this flow passage. After leaving the air-inducing tube, the air gives an impingement to the closed end of the fuel cell and then flows backward to the outside. In this pathway, the air obtains heat from the heat-generating fuel cell tube and transfers this heat to the cold air in the air-feeding tube. It is easy to understand that the electrochemical reaction at the closed end of the fuel cell is strong because the concentrations of fuel and air are both high there. Therefore, the heat generation due to Joule heating and entropy change of the electrochemical reaction is higher at the upstream of the fuel path. However, the fuel cell closed end does not have the highest temperature, therefore, it is believed that the cooling of air to the closed end of the fuel cell is responsible for this. After being heated at the closed-end region, air temperature is high and its cooling ability for the cell tube is low when it is in the annulus between the air-inducing tube and the cell tube. At the cell open-end region, the air in the annulus can transfer heat to the incoming cold fresh air in the air-inducing tube and this will help it to cool the fuel cell tube. From this air flow arrangement, the hotspot temperature of the cell tube might mostly occur in the center of the longitudinal direction of the cell tube. The air flow has two passes, incoming in the air-inducing tube and outgoing in the annulus between the air-inducing tube and cell tube, therefore, the heat exchange in between the two passes allows the air to mitigate its temperature fluctuation along the whole air path and thus the temperature field in the fuel cell might be maintained relatively uniform. Nevertheless, the heat generation, air and fuel temperature and air-cooling to the fuel cell will collectively affect the temperature field in the fuel cell. Thus, the hotspot position in a cell tube might shift more or less away from the center region depending on the operating condition of the fuel cell.

Fig. 10 shows the gas species' molar fraction contours in even-difference for the same SOFC under the same operating condition as discussed in Fig. 9. In the air path, oxygen consumption at the cell closed-end region is relatively large, which leads to more dense contour lines. The contour shape of oxygen also indicates a relatively large difference of the molar fraction between the bulk flow and the wall of cathode/air interface. This also implies that the mass transport resistance on airside might be dominant in lowering the cell performance. Feeding more air than needed is the way already well accepted to in fuel cell technology.

The consumption by electrochemical reaction and generation from water-shift of CO collectively determines the hydrogen budget. Since the consumption takes the upper hand, the hydrogen molar fraction decreases along the fuel stream. Corresponding to this situation for hydrogen, the consumption due to water-shift and production due to electrochemical reaction makes the water vapor increase gradually along the fuel stream. The water-shift of CO proceeds gradually along the fuel path, and thus the mole fraction of CO decreases and the CO_2 increases. The shape of the contour lines of the

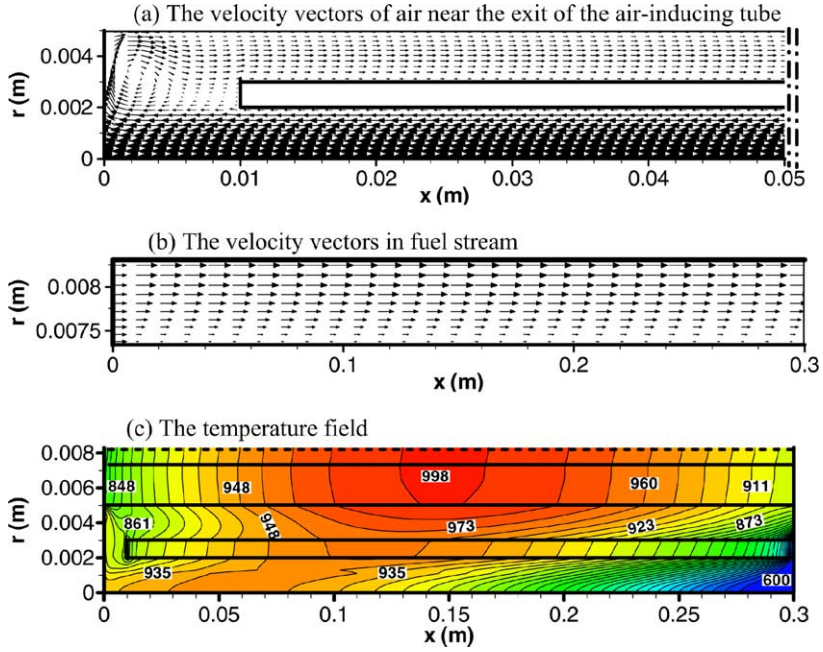

Fig. 9. Simulation results of the flow and temperature fields for the cell tested by Hirano et al. [7]. (Cell current density is 185 mA/cm^2.)

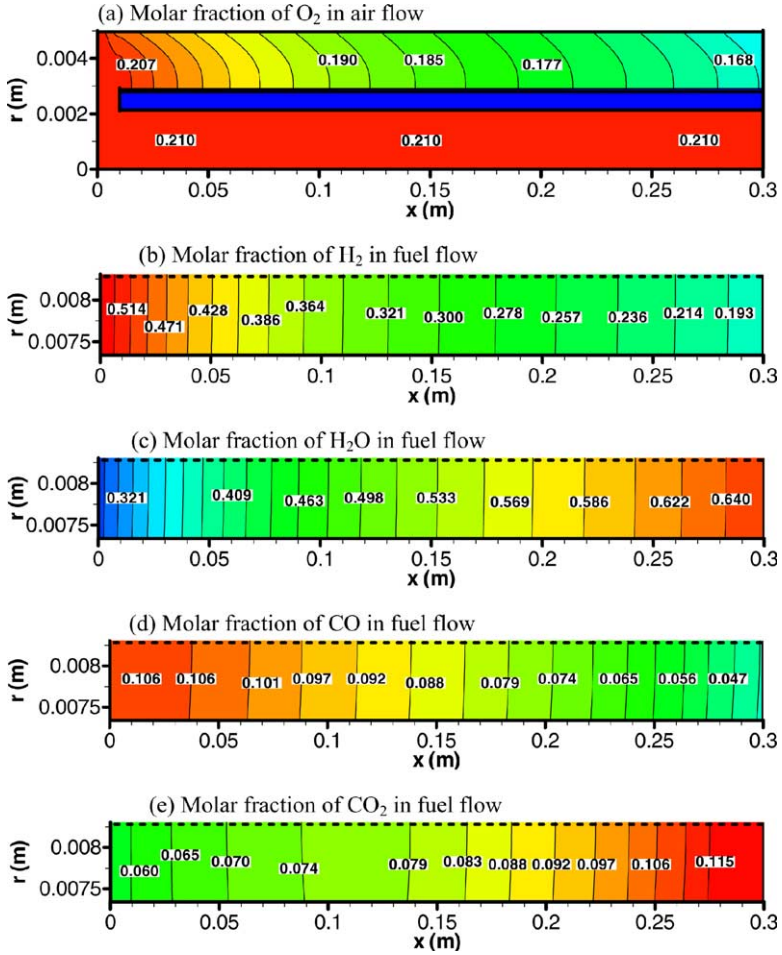

Fig. 10. Simulation results of the species' molar fraction contours for the cell tested by Hirano et al. [7]. (Cell current density is 185 mA/cm^2.)

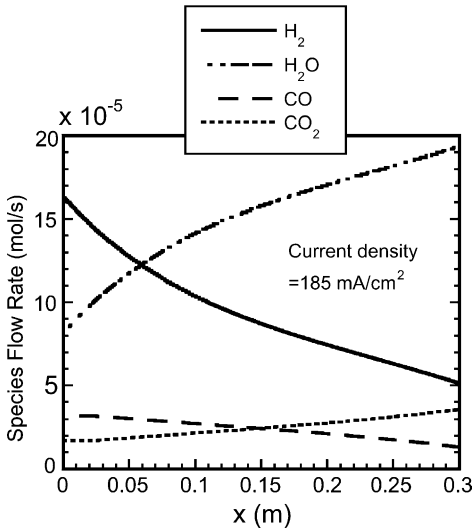

Fig. 11. Simulation results of species' molar flow rate varying in the fuel channel for the cell tested by Hirano et al. [7]. (Cell current density is 185 mA/cm^2.)

species in the fuel path is relatively flat from the cell wall to the bulk flow. This is an indication that mass diffusion in the fuel channel is relatively strong. For further understanding of the variation of the gas species, Fig. 11 shows their molar flow rate variation along the fuel path. In one third of the length from fuel inlet, the hydrogen flow rate shows a faster decrease and the water flow rate shows a faster increase, indicating a stronger reaction in the upstream. The flow rate of CO and CO_2 vary roughly in a linear style and a small amount of CO still exists in the waste gas.

4. Conclusion

The present model assumed that the heat and mass species do not exchange in between one cell and its neighboring cells when the tubular SOFCs is working in a cell stack. A surrounding fuel flow space controllable by the interested cell was then outlined, for which zero heat and mass fluxes were assumed at the boundary in the neighborhood with other cells. A two-dimensional numerical model for the flow, heat/mass transfer and chemical/electrochemical performance in such a cell operating in a stack was developed. Numerical simulation was conducted for three different tubular SOFCs having practical operational results published by different researchers. The model-predicted cell voltage agrees with the experimental data with a deviation of less than 7.4% for all the experimental data. The fuel cell temperature from the prediction also agrees with the test data satisfactorily.

It was found that the two ends of fuel cell have a relatively low temperature. The hotspot locates closer to the closed end of the cell tube when the operating current density is low. With increasing current density, the hotspot shifts to the open-end side of the cell and also the hotspot temperature decreases which makes the uniformity of temperature distribution better along the fuel cell tube. The molar fraction contour of oxygen in the air channel shows a large difference in the oxygen concentration between the bulk air flow and the cathode/air interface. In the fuel channel, the species molar fraction contour lines are rather flat, showing a relatively smaller difference between bulk flow and the anode/fuel interface.

References

[1] S. Srinivasan, R. Mosdale, P. Stevens, C. Yang, Annu. Rev. Energy Environ. 24 (1999) 281–328.
[2] F.J. Gardner, Proc. Inst. Mech. Eng. A 211 (1997) 367–379.
[3] S.P. Harvey, H.J. Richter, ASME J. Energy Resour. Technol. 116 (1994) 312–318.
[4] K. Suzuki, H. Iwai, J.H. Kim, P.-W. Li, K. Teshima, Proceedings of the 12th International Heat Transfer Conference, Grenoble, 18–23 August 2002, vol. 1, 2002, pp. 403–414.
[5] E.F. Sverdrup, C.J. Warde, R.L. Eback, Energy Convers. 13 (1973) 129–136.
[6] N.F. Bessette, W.J. Wepfer, Trans. ASME J. Energy Resour. Technol. 117 (1995) 43–49.
[7] A. Hirano, M. Suzuki, M. Ipponmatsu, J. Electrochem. Soc. 139 (1992) 2744–2751.
[8] P. Aguiar, D. Chadwick, L. Kershenbaum, Chem. Eng. Sci. 57 (2002) 1665–1677.
[9] J.R. Ferguson, J.M. Fiard, R. Herbin, J. Power Sources 58 (1996) 109–122.
[10] W.M. Kays, M.E. Crawford, Convective Heat and Mass Transfer, third ed., McGraw-Hill, New York, 1993.
[11] P.-W. Li, L. Schaefer, Q.M. Wang, M.K. Chyu, in: Paper Presented at the ASME International Mechanical Engineering Congress and Exposition, Paper No. IMECE2002-32564, 17–22 November 2002, New Orleans, LA, USA.
[12] E.A. Liese, R.S. Gemmen, F. Jabbari, J. Brouwer, in: Proceedings of the International Gas Turbine and Aero-engine Congress and Exhibition, Indianapolis, IN, USA, ASME Paper 99-GT-360, 1999.
[13] S.H. Chan, K.A. Khor, Z.T. Xia, J. Power Sources 93 (2001) 130–140.
[14] S. Ahmed, C. McPheeters, R. Kumar, J. Electrochem. Soc. 138 (9) (1991) 2712–2718.
[15] A.F. Massardo, F. Lubelli, Paper Presented at the International Gas Turbine and Aero-engine Congress and Exhibition, Paper No. 98-GT-577, 1998.
[16] R.H. Perry, D.W. Green, Perry's Chemical Engineer's Handbook, seventh ed., McGraw-Hill, New York, 1986.
[17] P.F. Incropera, D.P. DeWitt, Introduction to Heat Transfer, third ed., Wiley, New York, 1996.
[18] S.V. Patankar, Numerical Heat Transfer and Fluid Flow, McGraw-Hill, New York, 1980.
[19] K.C. Karki, S.V. Patanka, AIAA J. 27 (9) (1989) 1167–1174.
[20] C. Beckermann, T.F. Smith, J. Numer. Heat Transfer, Part B 23 (1993) 127–133.
[21] E.R.G. Eckert, R.M. Drake, Heat and Mass Transfer, McGraw-Hill, New York, 1959.
[22] A. Hagiwara, H. Michibata, A. Kimura, M.P. Jaszcar, G.W. Tomlins, S.E. Veyo, in: Proceedings of the Third International Fuel Cell Conference, D2–4, 1999, pp. 365–368.
[23] S.C. Singhal, Electrochem. Soc. Proc. 19-99 (1999) 39–51.
[24] S.C. Singhal, Solid State Ionics 135 (2000) 305–313.
[25] G.W. Tomlins, M.P. Jaszar, in: Proceedings of the Third International Fuel Cell Conference, D2–4, 1999, pp. 369–372.